



Efficient photochemical water splitting and organic pollutant degradation by highly ordered TiO₂ nanopore arrays

Yanbiao Liu, Baoxue Zhou^{*}, Jing Bai, Jinhua Li, Jialing Zhang, Qing Zheng, Xinyuan Zhu, Weimin Cai

School of Environmental Science and Engineering, Shanghai Jiaotong University, No. 800 Dongchuan Rd, Shanghai, China

ARTICLE INFO

Article history:

Received 7 October 2008

Received in revised form 18 November 2008

Accepted 29 November 2008

Available online 6 December 2008

Keywords:

TiO₂ nanopore arrays

Water splitting

Organic compound degradation

ABSTRACT

We synthesized highly ordered TiO₂ nanopore arrays (TNPs) with controllable pore size and good uniformity by anodization at low temperature in fluorinated dimethyl sulfoxide (DMSO) solution with a post-sonication treatment. TNPs possess excellent separation and transport properties of photo-generated electron/hole pair and hence reveal enhanced photocurrent response and photochemical properties for water splitting and organic compound degradation. The TNPs present maximum photo-conversion efficiency for water splitting of 0.28% under AM1.5 irradiation. This value compares favorably with a maximum photo-conversion efficiency of 0.21% for TiO₂ nanotube arrays (TNAs) under the same conditions. When illuminated with 1.0 mW cm⁻² UV light, the maximum photo-conversion efficiency can be increased to 22% for TNPs, which is 5% higher than TNAs. The kinetic constant of photoelectrocatalytic (PEC) degradation of methyl orange (MO) for TNPs is found to be 1.27 times as high as that for TNAs when biased at 0.5 V. The visible light response of TNPs might be further improved by relevant surface modification technology.

© 2008 Elsevier B.V. All rights reserved.

1. Introduction

Since the first report [1] on the photochemical splitting of water on a n-TiO₂ electrode by Fujishima and Honda, extensive research has shown that titania is an excellent catalyst due to its unique structure, remarkable properties and wide range of potential applications in water splitting, degradation of organic pollutants, photovoltaic cells and other fields. Although TiO₂ has several advantages as described above, it has two critical limitations [2]: the high rate of electron/hole pair recombination among TiO₂ particles as well as the poor activation of TiO₂ by visible light. In response to these deficiencies, most attempts [3–5] at synthesizing new TiO₂ structures, like TiO₂ nanowires, nanorods, nanobelts, nanorings, nanotubes, etc., or attempts at modifying TiO₂ by depositing noble metal on its surface, sensitizing it with dyes, or doping it with transition metals or non-metal elements and complexes with matching semiconductors, in order to decrease the recombination between photo-generated charges and improve its absorption in the visible region of the solar spectrum, have met with certain success. Therefore, to fabricate a TiO₂ material with a faster electron transport and lower recombination rate is a key issue for its photochemical applications. In 1999, Zwillig et al. [6] reported the formation of TiO₂ nanotube layers by anodization in

HF containing electrolyte. In 2001, Gong et al. [7] prepared highly ordered TiO₂ nanotube arrays (TNAs) about 500 nm in length by potentiostatic anodization of titanium in HF aqueous solution. Subsequently, the length of the nanotube arrays increased to a few micrometers by tuning the pH of the [F⁻] containing electrolyte solution [8]. This was then followed by the use of polar organic electrolytes, where the tube length can be extended to more than 700 μm [9]. The well-aligned nanotubular microstructures are perpendicular to the electrically conductive Ti substrate, forming a Schottky-type contact and providing a unidirectional electrical channel for the transport of photo-generated electrons [10]. Hence, the nanotube film reveals good charge transport properties as well as elevated photoelectrical and electrochemical performances. For instance, the photo-conversion efficiency of dye-sensitized TNAs solar cells has reached 5.44% [11,12] and reached 16.25% for hydrogen generation by employing the water splitting reaction under UV irradiation [13]. The degradation rate of pentachlorophenol on TNAs is found to be 1.86 times faster than on traditional TiO₂ films [14]. In our recent work [15], the TNAs-based chemical oxygen demand (COD) sensor can achieve rapid and accurate COD determination of wastewater.

Recently, we developed a novel kind of TiO₂ nanopore arrays (TNPs) microstructures [16] with a controllable pore size and good uniformity. Compared with TNAs, the TNPs not only possess excellent separation and transport properties of photo-generated electron/hole pair and strong mechanical stability, but also reveal outstanding photochemical performance. To the best of our

^{*} Corresponding author. Tel.: +86 21 5474 7351; fax: +86 21 5474 7351.
E-mail address: zhoubaoxue@sjtu.edu.cn (B. Zhou).

knowledge, no study has been reported to date regarding such Ti-based nanoporous material. In this work, we report on the preparation and characterization of TNPs, and compare the use of TNPs and TNAs electrodes in photochemical applications such as water splitting and organic compound degradation.

2. Experimental

2.1. Preparation of TNPs

During a typical fabrication process of highly ordered TNPs, titanium sheets (0.25 mm thick, 99.9% purity), cut into samples of size 2 cm × 5 cm, were degreased by sonicating in 1:1 acetone and ethanol, followed by rinsing with DI water and dried in a stream of air. Electrochemical anodization of titanium was carried out using a DC power supply (TRADEX, 0–5 A, 0–60 V) to control the experimental current and voltage. All anodization experiments were carried out with vigorous magnetic agitation at 5 °C in a two-electrode system (4 cm separation). The TNPs can be fabricated by a two-step process: after anodization in dimethyl sulfoxide (DMSO, ≥99.8%) containing 5% HF solution (≥40 wt%), the TNPs were post-sonicated for 10 min to remove the uppermost film completely. The obtained TNPs, which are initially amorphous, need to be crystallized by annealing in an air atmosphere for 8 h at 450 °C with heating and cooling rates of 1 °C/min. As a comparison, a low-voltage anodization step (20 V for 30 min) in a 0.5 wt% HF aqueous solution was adopted to synthesize a TNAs film of about 500 nm in length [7,17].

2.2. Characterization of TNPs

The morphologies of the TNPs were studied using a field emission scanning electron microscope (PHILIPS, Netherlands, Sirion200) equipped with an energy dispersive X-ray spectroscopy (OXFORD, U.K.). The pore depth of the TNPs samples can be measured by tapping mode atomic force microscopy (BioScope) from Veeco Instruments Inc. (USA). An X-ray diffractometer

(BRUKER AXS-8 ADVANCE) was used to determine the crystalline structure of the samples. The composition of the nanopore arrays were analyzed with X-ray photoelectron spectroscopy (VG Microlab 310F, Al K α radiation).

2.3. Electrochemical characterization

The photochemical experiments were carried out in a rectangular shaped quartz reactor (20 mm × 40 mm × 50 mm) using a three-electrode system with a platinum foil counter electrode, a saturated Ag/AgCl reference electrode and a TiO₂ work electrode. The supply bias and work current were controlled using a CHI electrochemical analyzer (CHI 660C, CH Instruments, Inc., USA). A 500 W Xe lamp (Shanghai Hualun Bulb Factory) was used as the simulated solar light and a 4 W UV lamp (GE, Japan G4T5) with central wavelength 254 nm was chosen as a UV light source. The photoelectrocatalytic (PEC) degradation of methyl orange (MO) experiment was performed under the following conditions: UV irradiation (1.0 mW cm⁻² light intensity), vigorous stirring, 0.5 V (vs. Ag/AgCl) of electric bias, pH 5.5, 0.01 mol L⁻¹ sodium sulfate as electrolyte, and no airflow. The photocatalytic (PC) oxidation reaction was performed by using the same set-up without applying an external potential on the functional electrodes. The initial concentration of MO solution was 20 mg L⁻¹ and the reaction solution was 25 mL during the experiment. At different time intervals, the reaction solution was analyzed using a UV–vis spectrophotometer (UV2102 PCS, UNICO, Shanghai) at a wavelength of 462 nm.

3. Results and discussion

Fig. 1a–c presents the field emission scanning electron microscopy (FESEM) images of unannealed TNPs sample anodized at 40 V (vs. Pt) in fluorinated DMSO solution at 5 °C for 20, 50 and 70 h, respectively. It was found that within 20 h, the surface revealed a discrete porous structure, as shown in Fig. 1a. After 50 h, a continuous nanoporous structure, of uneven diameters, dis-

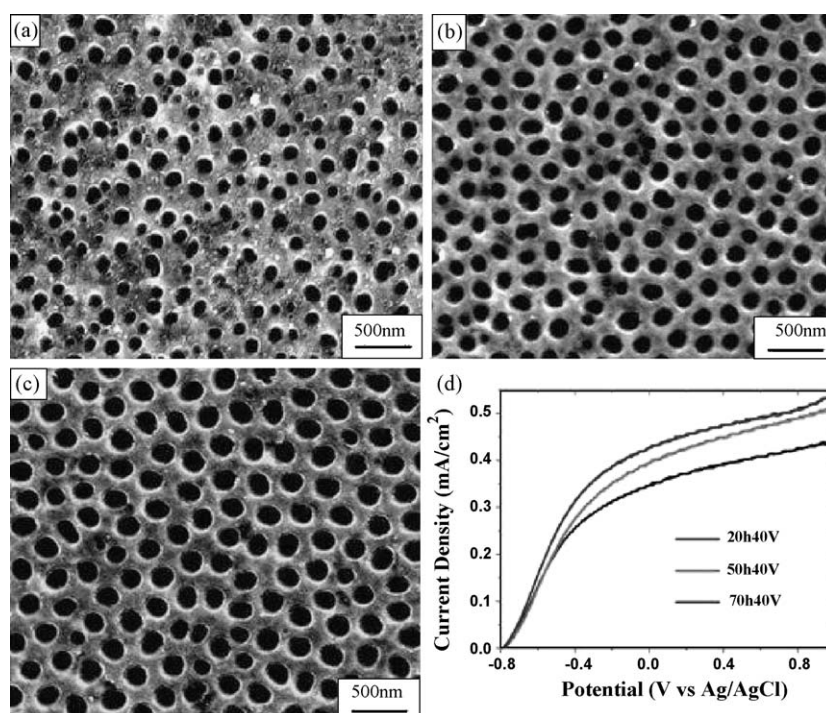


Fig. 1. FESEM top-view images of unannealed TNPs samples anodized in fluorinated DMSO electrolyte solution at 40 V for different times: (a) 20 h, (b) 50 h and (c) 70 h. (d) Variation of photocurrent density vs. measured potential for the above three TNPs samples (after annealing) in 1 M KOH electrolyte solution under AM1.5 irradiation.

tributed on a honeycomb-like mesh emerged from the surface of the sample. With further anodization (Fig. 1c), the highly ordered TNPs formed scallop-like shapes with homogeneous pore diameters. For Ti anodization over, respectively, 20, 50 and 70 h, an increase in average pore diameter from ~ 90 to ~ 220 nm was observed. However, the formation mechanism of TNPs was still unclear, which may be attributed to the effect of anodization in low temperature and the sonication treatment. The photocurrent densities of the as-annealed TNPs anodized for different anodization times in 1 M KOH electrolyte solution as a function of applied potential under AM1.5 irradiation (light intensity of 100 mW cm^{-2}) are shown in Fig. 1d. As can be seen, the flat band potential was about -0.78 V (vs. Ag/AgCl), which is independent of the anodization period. However, the current density at more positive potentials was a function of the anodization time. A maximum photocurrent density of 0.55 mA cm^{-2} was gained for the TNPs sample anodized for 70 h.

Fig. 2a and b presents the FESEM images of TNAs prepared by Ti anodization in 0.5 wt% HF aqueous solutions at 20 V for half an hour,

Table 1Dimensional data of as-prepared TiO_2 photoanodes.

Photoanode	Φ_{outer} (nm)	Φ_{inner} (nm)	Length (depth, nm)	S (nm^2)
TNPs	220	–	55	2.96×10^5
TNAs	100	70	500	3.20×10^6

about 500 nm in length and 100 nm in diameter. For measurement purpose, the TNPs material was treated as “semi-ellipsoid” and the TNAs were treated as “cylinder”. As for the nanoporous microstructure, the specific surface area was calculated with matlab function: $S = m\text{fun}(\text{'ellipsoid'}, x, y, z)/2 \times N + \text{void area among the pores}$, here x, y, z are the mean length of three “semi-axes”, and N is the number of the tubes within $500 \text{ nm} \times 500 \text{ nm}$ area exposed to the illumination. The specific surface area of the tubelike structure within $500 \text{ nm} \times 500 \text{ nm}$ area were obtained in accordance with $S = \pi(\Phi_{\text{outer}} + \Phi_{\text{inner}}) \times L \times N$, where L is the thickness of the nanotube layer and N is the number of the tubes within $500 \text{ nm} \times 500 \text{ nm}$ area. The mean outer and inner diameter (Φ_{outer}

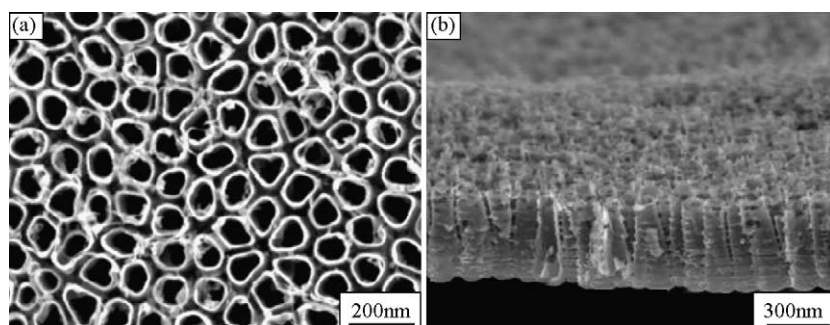


Fig. 2. FESEM images of TiO_2 nanotube arrays prepared in 0.5 wt% HF aqueous solution: (a) top-view and (b) cross-sectional view.

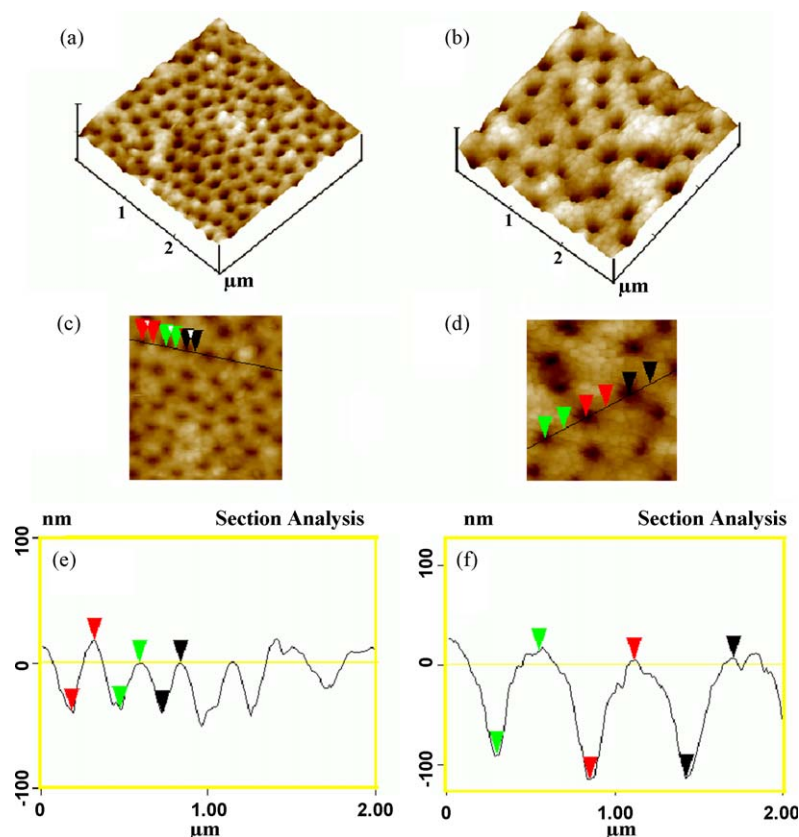


Fig. 3. TM-AFM images of TNPs samples grown from a 5 wt% HF–DMSO electrolyte solution at 5°C for 70 h at 40 V (a, c, and e) and 60 V (b, d, and f). 3D TM-AFM images are shown in a and b; 2D TM-AFM images are shown in (c) and (d); and section analysis of the TM-AFM images are given in (e) and (f).

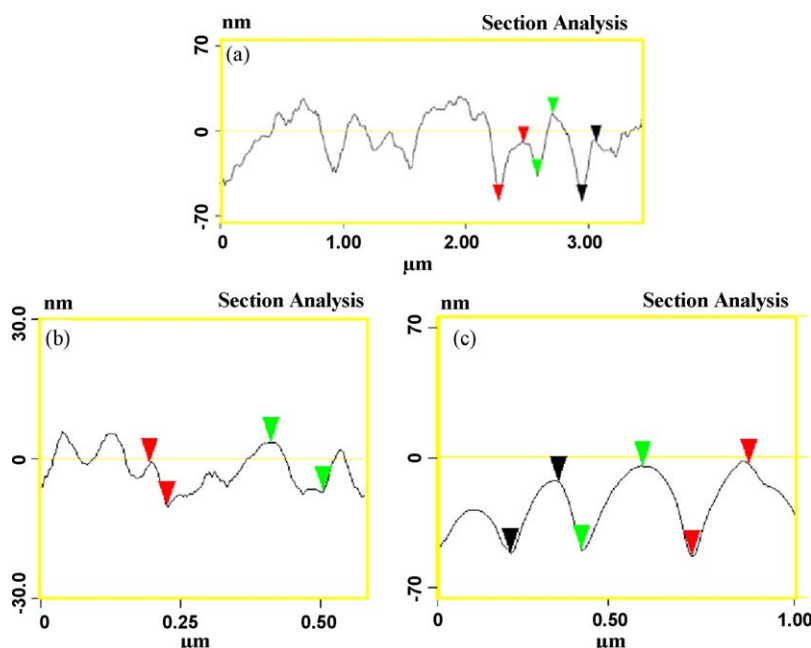


Fig. 4. TM-AFM images of TNPs sample grown in a 5 wt% HF–DMSO electrolyte at 20 V for 70 h (a) and at 40 V for 20 h (b) and 50 h (c).

and Φ_{inner}) of TNAs were measured from the FESEM images. The quantitative dimensional data of each as-prepared TiO_2 photoanodes were given in Table 1. The corresponding specific surface area is ranked as TNAs ($3.20 \times 10^6 \text{ nm}^2$) > TNPs ($2.96 \times 10^5 \text{ nm}^2$).

The pore depth of the TNPs samples prepared in 5 wt% HF–DMSO solution at 40 V (images a, c and e) and 60 V (images b, d and f) for 70 h was studied by tapping mode atomic force microscopy (TM-AFM), as shown in Fig. 3. Two 3D TM-AFM images (a and b) reveal a clear porous surface. Evidently, the pore diameter as well as the voids among the interpore areas for the sample prepared at 60 V is found to be much larger than its 40 V counterpart. The 2D TM-AFM images (c and d) display dense and uniform surface morphologies. The cross-section images (e and f) along the line given in images c and d show that the average pore depth for the 40 and 60 V samples was ~ 55 and ~ 100 nm, respectively. Fig. 4a presents the TM-AFM image of a TNPs sample after 70 h anodization at 20 V with a pore depth ~ 35 nm. As the applied potential was varied from 20 to 60 V, the pore depth for the TNPs anodized over a 70 h period increased from ~ 35 to ~ 100 nm.

Fig. 4b and c gives the TM-AFM images of a typical TNPs sample anodized in 5 wt% HF–DMSO electrolyte solutions at 40 V for 20 and 50 h, respectively. The resulting pore depth is ~ 10 and ~ 50 nm, respectively.

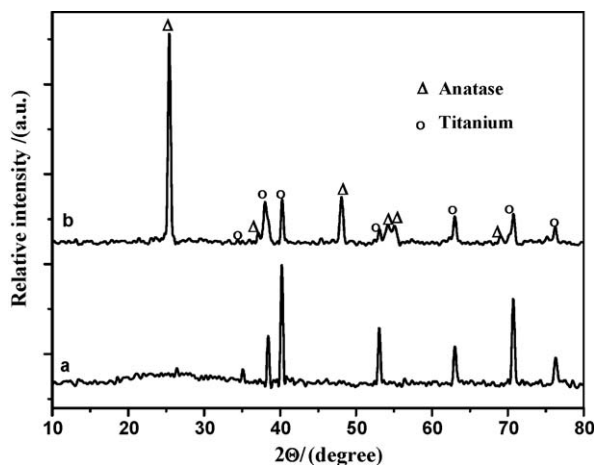


Fig. 5. XRD patterns of as-prepared TNPs before (curve a) and after annealing in air for 8 h (curve b) (both samples are anodized at 5°C for 70 h at 40 V in HF–DMSO solution).

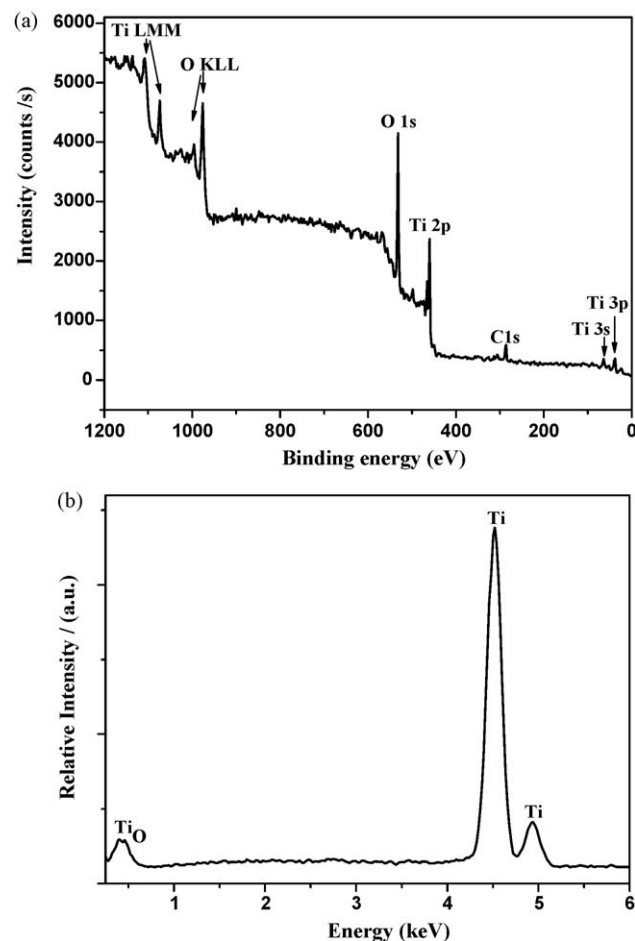


Fig. 6. The XPS survey (a) and EDX spectra (b) of the as-annealed TNPs sample anodized at 40 V for 70 h.

Fig. 5 compares the X-ray diffraction (XRD) patterns of a typical TNPs sample anodized for 70 h at 40 V taken before and after annealing at a temperature of 450 °C for 8 h in air. It can be seen that the annealing process transforms the as-prepared TNPs from an amorphous phase to anatase phase. The composition of the TNPs microstructure was determined by X-ray photoelectron spectroscopy (XPS) and energy dispersive X-ray (EDX). Fig. 6a is a survey (XPS) spectrum of the as-annealed TNPs sample anodized at 40 V for 70 h. Fig. 6b shows the EDX spectra of the composition of the same sample. It can be seen that the TNPs sample is consist of Ti and O.

Fig. 7a gives a comparison of the variation of photocurrent density (which corresponds to the rates of production for hydrogen and oxygen) vs. measured potential (vs. Ag/AgCl) in 1 M KOH solution under AM1.5 irradiation for as-annealed TNPs and TNAs,

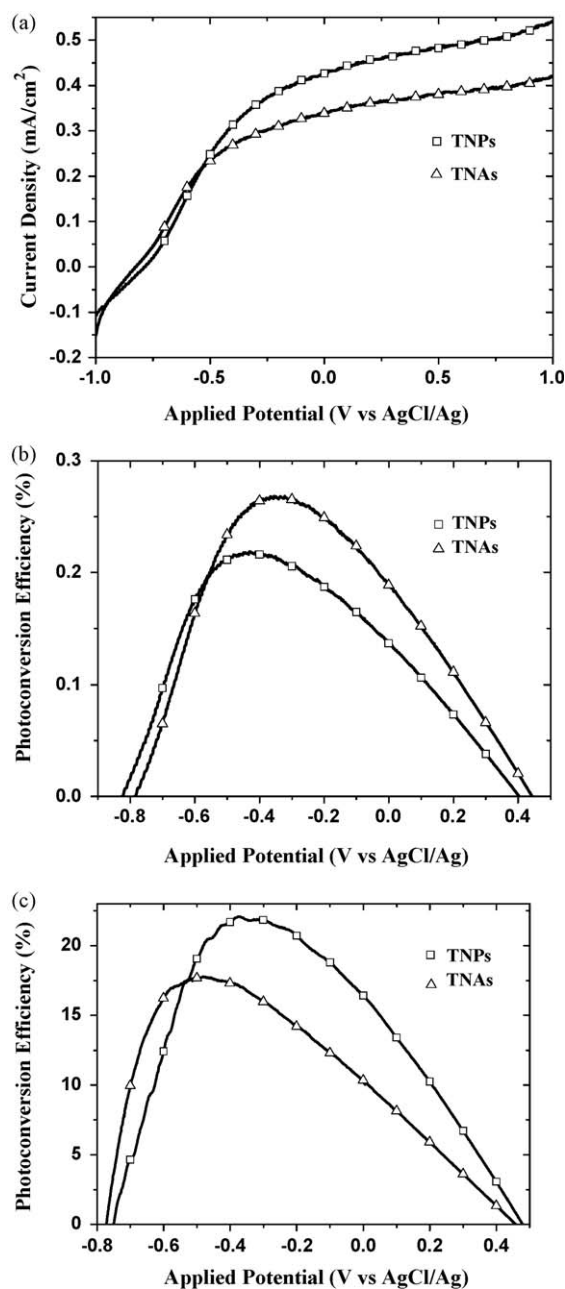


Fig. 7. (a) Photocurrent density generated from as-annealed TNPs and TNAs in 1 M KOH electrolyte solution under AM1.5 irradiation. Photo-conversion efficiency as a function of measured potential (vs. Ag/AgCl) for as-annealed TNPs and TNAs under AM1.5 irradiation (b) and 1.0 mW cm⁻² UV illumination (c).

respectively. The maximum photo-conversion efficiency of 0.28% for TNPs (Fig. 7b) was observed at an applied potential of -0.35 V with a photocurrent density of 0.34 mA cm⁻². However, under the same illumination, a maximum photo-conversion efficiency of 0.21% was observed at a bias of -0.4 V for TNAs. At an applied potential of 1.0 V, the photocurrent density of TNPs was more than 28% higher than the value for TNAs. When illuminated with 1.0 mW cm⁻² UV light, the maximum conversion efficiency of 22% can be obtained for TNPs, which is 5% higher for TNAs under the same conditions of illumination (Fig. 7c). The enhanced photo-

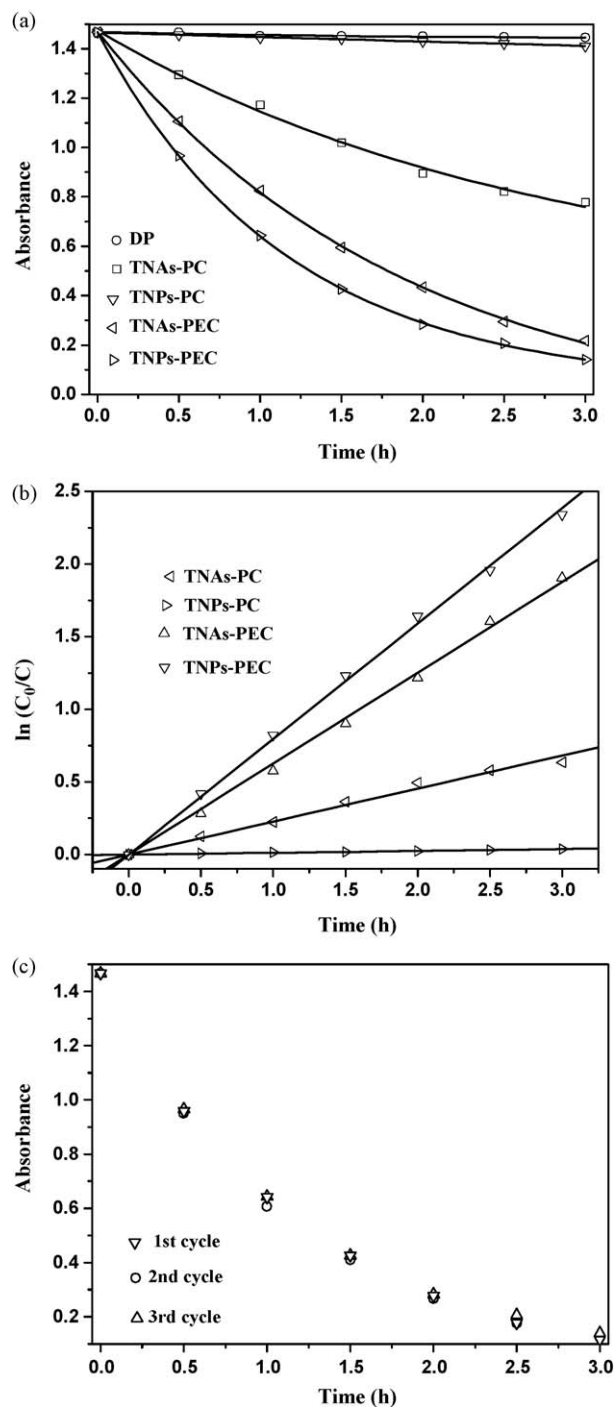


Fig. 8. (a) The PEC, PC and direct photolysis (DP) of MO solutions by TNPs and TNAs; (b) comparison of PC and PEC kinetic curves of MO by TNAs and TNPs electrode and (c) variation of the MO concentration in PEC degradation by the TNPs in three PEC cycles.

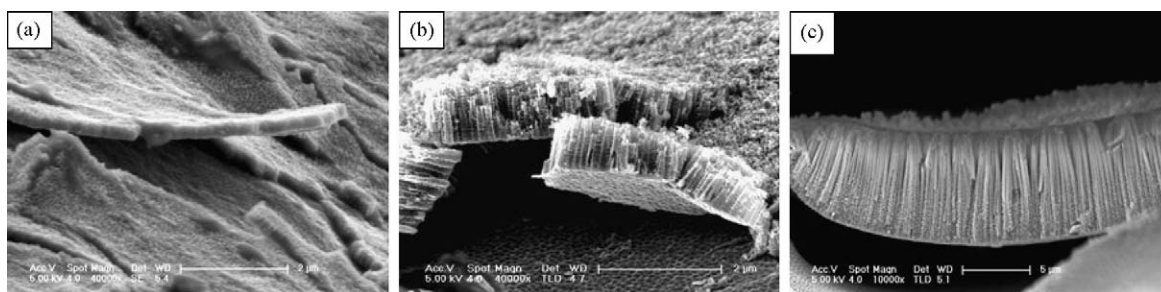


Fig. 9. FESEM images of TiO₂ nanotube arrays fabricated by Ti anodization in different electrolyte solutions when undergone a post-sonication treatment for a few seconds.

current response of TNPs means the electron/hole pair induced by simulated solar light (or UV light) might split and transport more readily within TNPs. The photo-conversion efficiency, η , is calculated as [13,18]

$$\eta (\%) = j_p \left[\frac{(E_{\text{rev}}^0 - |E_{\text{app}}|)}{I_0} \right] \times 100 \quad (1)$$

where j_p is the photocurrent density (mA cm^{-2}), $j_p E_{\text{rev}}^0$ is the total power output, $j_p |E_{\text{app}}|$ is the electrical power input, and I_0 is the power density of incident light (mW cm^{-2}). E_{rev}^0 is the standard reversible potential, which is 1.23 V for water splitting reaction, and the applied potential is $E_{\text{app}} = E_{\text{meas}} - E_{\text{aoc}}$, where E_{meas} is the electrode potential (vs. Ag/AgCl) of the working electrode at which photocurrent was measured under illumination and E_{aoc} is the electrode potential (vs. Ag/AgCl) of the same working electrode under open circuit conditions, under the same illumination, and in the same electrolyte. The voltage at which the photocurrent becomes zero was taken as E_{aoc} .

The favorable electron separation and transport properties in TNPs is further supported by organic compound degradation experiments. The PC, photoelectrocatalytic (PEC, PC with bias potential), and direct photolytic (DP) degradation of MO in aqueous solutions were performed under given conditions on annealed TNPs and TNAs, respectively. It can be seen in Fig. 8a that both TNPs and TNAs reveal similar reaction characteristics: $\text{PEC} > \text{PC} > \text{DP}$, but the catalytic characteristics of TNPs and TNAs were much different. The TNPs with smaller specific surface area show a higher PEC degradation efficiency with a reaction rate constant of 0.7952 h^{-1} (Fig. 8b). However, the TNAs with larger specific surface areas only show a reaction rate constant of 0.6257 h^{-1} under the same conditions. The kinetic constant of PEC degradation of MO for TNPs is found to be 1.27 times higher than that for the TNAs. MO removal reaches 92% for TNPs after 3 h PEC reaction, which is higher than the 85% obtained for TNAs. However, the dependence of the reactivity on the specific surface area of the materials is exactly opposite to that in the PC process. In the PC degradation of MO, the increased specific surface area of the TNAs material improves its PC reactivity greatly. Nevertheless, the TNPs reveal very weak PC reactivity and only 3.8% MO was degraded over a period of 3 h, which is much lower than 47% for TNAs under the same conditions. The rate constants for TNPs and TNAs are 0.0128 and 0.225 h^{-1} , respectively. The increased specific surface area favors light trapping, which results in more photo-generated electron/hole pair and an enhanced PC reactivity [10]. This result demonstrates that the separation and transport of photo-generated charges was not dependent on the specific surface area of TiO₂ materials when under a biased potential. The TNPs with smaller surface area reveals even higher photochemical properties for organic compound degradation. This means that in the PC process, the specific surface area of the electrode materials is the most important parameter. However, in the PEC process, the

applied positive bias plays a dominant role in the MO degradation rather than the specific surface area of the electrode materials. We also study the stability of the TNPs electrode for the PEC degradation of MO by reusing this electrode in three PEC cycles. As given in Fig. 8c, the experimental data for MO degradation curve are obviously reproducible in three PEC cycles.

The properties of functional materials are highly dependent on their microstructure and mechanical stability. Within TNPs, the porous structure is directly connected to the Ti substrate, which avoids the binding between the nanotube layers and the substrate as observed in TNAs. Hence, the TNPs combine with the substrate more directly and with a greater compactness, resulting in a lower transport resistance for photo-generated electrons. The nanoporous microstructure can greatly improve the separation and transport efficiency of photo-generated charge carriers with a lower recombination rate. Meanwhile, such microstructures also favor a lessening of the change of internal stress caused by external mechanical forces or a lessening of the change in environmental temperature. In addition, such microstructures also show improved mechanical stability, since the TiO₂ is directly attached to the pore walls and there are more supporting points in the nanoporous structure.

However, within nanotubular materials, the attachment between the nanotube film and the substrate is weak [19]. It is common for nanotubes, especially for long nanotubes, to tilt, rupture or even peel off the substrate when an external mechanical force is applied to the surface of the film. The tilting, rupturing or peeling of the nanotubes also readily occur when there is a change in environmental temperature because of the different internal stress of Ti and TiO₂ caused by their different expansion coefficients. These will inevitably influence their mechanical stability as well as the separation and transport of photo-generated electron/hole pair. Fig. 9 presents the FESEM images for nanotube films prepared by Ti anodization in different electrolyte solutions to tilt or rupture when undergone a post-sonication treatment for a few seconds. Fig. 9a is the nanotube film anodized in 0.5 wt% HF aqueous solution for 1 h period with a thickness about 500 nm. Fig. 9b gives the nanotubes fabricated at 20 V for 8 h in an electrolyte containing 0.1 M KF, 1 M NaHSO₄ and 0.2 M trisodium citrate, with sodium hydroxide added to adjust the pH to 4.0. The as-prepared TNAs were about 1.5 μm in length. Fig. 9c shows the FESEM image for Ti anodization in 5 wt% HF-DMSO electrolyte at 40 V for 20 h at 30 °C. The resulted TNAs were about 9 μm in length.

4. Conclusions

In conclusion, we have demonstrated certain progress toward the goal of enhancing the photochemical reactivity as well as the mechanical stability of TiO₂ nanofilms by using highly ordered titania nanopore arrays as the photoanode. By changing the anodizing time and applied potential, one can control the TNPs parameters like pore diameter and depth. The special microstruc-

ture of TNPs possess superior separation and transport properties of photo-generated electron/hole pair. The enhanced reactivity in water splitting and dye effluent decoloration is obtained for TNPs. Therefore, such kinds of film material with high PEC reactivity and strong stability will have many potential applications in various fields as an outstanding photoanode material.

Acknowledgments

The authors would like to acknowledge the National Nature Science Foundation of China (No. 20677039), the State Key Development Program for Basic Research of China (Grant No. 2009CB220004), the Shanghai Basic Research Key Project (08JC1411300) and the Program of New Century Excellent Talents in University (No. NCET-04-0406) for financial support.

Appendix A. Supplementary data

Supplementary data associated with this article can be found, in the online version, at [doi:10.1016/j.apcatb.2008.11.034](https://doi.org/10.1016/j.apcatb.2008.11.034).

References

- [1] A. Fujishima, K. Honda, *Nature* 238 (1972) 37–39.
- [2] J.H. Park, S. Kim, A.J. Bard, *NanoLett.* 6 (2006) 24–28.
- [3] R. Beranek, H. Kisch, *Electrochem. Commun.* 9 (2007) 761–766.
- [4] Y. Wang, G. Du, H. Liu, D. Liu, S. Qin, N. Wang, C. Hu, X. Tao, J. Jiao, J. Wang, Z.L. Wang, *Adv. Funct. Mater.* 18 (2008) 1131–1137.
- [5] B. O'Regan, M. Gratzel, *Nature* 353 (1991) 737–740.
- [6] V. Zwillling, E. Darque-Ceretti, A. Boutry-Forveille, D. David, M.Y. Perrin, M. Aucouturier, *Surf. Interface Anal.* 27 (1999) 629–637.
- [7] D.W. Gong, C.A. Grimes, O.K. Varghese, W.C. Hu, R.S. Singh, Z. Chen, E.C. Dickey, *J. Mater. Res.* 16 (2001) 3331–3334.
- [8] J.M. Macak, H. Tsuchiya, L. Taveira, S. Aldabergerova, P. Schmuki, *Angew. Chem. Int. Ed.* 44 (2005) 7463–7465.
- [9] H.E. Prakasham, K. Shankar, M. Paulose, O.K. Varghese, C.A. Grimes, *J. Phys. Chem. C* 111 (2007) 7235–7241.
- [10] Z.Y. Liu, X.T. Zhang, S. Nishimoto, M. Jin, D.A. Tryk, T. Murakami, A. Fujishima, *J. Phys. Chem. C* 112 (2008) 253–259.
- [11] G.K. Mor, O.K. Varghese, M. Paulose, K. Shankar, C.A. Grimes, *Solar Energy Mater. Solar Cells* 90 (2006) 2011–2075.
- [12] Y.B. Liu, B.X. Zhou, B.T. Xiong, J. Bai, L.H. Li, *Chin. Sci. Bull.* 52 (2007) 1585–1589.
- [13] M. Paulose, K. Shankar, S. Yoriya, H.E. Prakasham, O.K. Varghese, G.K. Mor, T.A. Latempa, A. Fitzgerald, C.A. Grimes, *J. Phys. Chem. B* 110 (2006) 16179–16184.
- [14] X. Quan, S.G. Yang, X.L. Ruan, H.M. Zhao, *Environ. Sci. Technol.* 39 (2005) 3770–3775.
- [15] Q. Zheng, B.X. Zhou, J. Bai, L.H. Li, Z.J. Jin, J.L. Zhang, J.H. Li, Y.B. Liu, W.M. Cai, X.Y. Zhu, *Adv. Mater.* 20 (2008) 1044–1049.
- [16] B.X. Zhou, Y.B. Liu, J. Bai, J.H. Li, Chinese Patent Application No. 200810033302.3.
- [17] J. Bai, B.X. Zhou, L.H. Li, Y.B. Liu, Q. Zheng, X.Y. Zhu, W.M. Cai, J.S. Liao, L.X. Zou, *J. Mater. Sci.* 43 (2008) 1880–1884.
- [18] S.U.M. Khan, M. Al-Shahry, W.B. Ingler Jr., *Science* 297 (2002) 2243–2245.
- [19] S. Yoriya, M. Paulose, O.K. Varghese, G.K. Mor, C.A. Grimes, *J. Phys. Chem. C* 111 (2007) 13770–13776.